Correlating CFD Simulation With Wind Tunnel Test for the Full-Scale UH-60A Airloads Rotor

Ethan Romander
ethan.romander@nasa.gov

Thomas R. Norman
tom.norman@nasa.gov

I-Chung Chang
i.c.chang@nasa.gov

Flight Vehicle Research and Technology Division
NASA Ames Research Center
Moffett Field, CA

Abstract

Data from the recent UH-60A Airloads Test in the National Full-Scale Aerodynamics Complex 40- by 80- Foot Wind Tunnel at NASA Ames Research Center are presented and compared to predictions computed by a loosely coupled Computational Fluid Dynamics (CFD)/Comprehensive analysis. Primary calculations model the rotor in free-air, but initial calculations are presented including a model of the tunnel test section. The conditions studied include a speed sweep at constant lift up to an advance ratio of 0.4 and a thrust sweep at constant speed into deep stall. Predictions show reasonable agreement with measurement for integrated performance indicators such as power and propulsive but occasionally deviate significantly. Detailed analysis of sectional airloads reveals good correlation in overall trends for normal force and pitching moment but pitching moment mean often differs. Chord force is frequently plagued by mean shifts and an overprediction of drag on the advancing side. Locations of significant aerodynamic phenomena are predicted accurately although the magnitude of individual events is often missed.

Notation

a_∞	freestream speed of sound
c	local chord length
f_c	force parallel to local chord line
f_n	force perpendicular to local chord line
m	moment about local quarter chord
A	total rotor disk area, $\pi R^2 = 2262$ ft^2
C_L	rotor lift coefficient, $\frac{L}{\rho(\Omega R)^2 A}$
C_P	rotor power coefficient, $\frac{P}{\rho(\Omega R)^3 A}$
C_{Pi}	induced power coefficient
C_{Po}	profile power coefficient
C_T	rotor thrust coefficient, $\frac{T}{\rho(\Omega R)^2 A}$
C_X	rotor propulsive force coefficient, $\frac{X}{\rho(\Omega R)^2 A}$

$M^2 c_c$	sectional chord force coefficient, $\frac{df_c/dr}{1/2\rho a_\infty^2 c}$
$M^2 c_n$	sectional normal force coefficient, $\frac{df_n/dr}{1/2\rho a_\infty^2 c}$
$M^2 c_m$	sectional pitching coefficient, $\frac{dm/dr}{1/2\rho a_\infty^2 c^2}$
M_{tip}	tip Mach number
L	rotor lift
N	number of blades, 4
P	total rotor power
R	rotor radius, 26.83 ft
T	rotor thrust
V_∞	freestream velocity
X	rotor propulsive force
α_c	wall corrected shaft angle
α_s	geometric shaft angle
μ	advance ratio, $\frac{V_\infty}{\Omega R}$
ψ	rotor azimuth, deg
ρ	freestream density
σ	rotor solidity, $\frac{N \cdot \bar{c}}{\pi R} = 0.0826$
Ω	rotor angular velocity

Figure 1 – UH-60A Airloads Rotor in 40- by 80-Foot Wind Tunnel.

Introduction

Testing was successfully completed in May 2010 on a full-scale UH-60A rotor system in the USAF's National Full-Scale Aerodynamics Complex (NFAC) 40- by 80-Foot Wind Tunnel [1]. The primary objective of this NASA/Army test program was to acquire a comprehensive set of validation-quality measurements on a full-scale pressure-instrumented rotor system at conditions that challenge the most sophisticated modeling and simulation tools. A secondary objective was to meet one of the original goals of the UH-60A Airloads program: to provide data to evaluate the similarity, or lack thereof, of measurements between small-scale wind tunnel [2], full-scale wind tunnel (current test), and full-scale flight test [3].

The test hardware included the same rotor blades used during the flight test. Figure 1 shows these blades installed on the NFAC Large Rotor Test Apparatus (LRTA) in the wind tunnel test section. Key measurements included rotor performance, blade loads, blade pressures, blade displacements, and rotor wake measurements using large-field Particle Image Velocimetry (PIV) and Retro-reflective Background Oriented Schlieren (RBOS).

Data were acquired over a wide range of test conditions, including speed sweeps at 1-g simulated flight conditions and parametric thrust sweeps (up to and including stall) at various combinations of shaft angles and forward speed. These conditions included airspeeds up to 175 kt and thrusts up to 32,000 lb. Data were also acquired

at matching conditions from the previous full-scale flight test and small-scale DNW wind tunnel test to assess rotor and wind tunnel scaling issues. Finally, unique slowed-rotor simulations were performed at reduced RPM (40% and 65%), achieving advance ratios up to 1.0. A complete enumeration of data acquired during the test is available in Ref. 1.

Unfortunately, not all test data is perfect and no simulation is exact. The goal of this work is to provide an initial correlation between measured data and a state of the art simulation. This correlation is intended to help discover flaws in experimental technique while at the same time identifying opportunities to enhance rotorcraft simulation technology.

Methodology

The complexity of rotorcraft aeromechanics is not easily modeled. The analytical results presented herein were obtained using two separate codes—each a specialist in a particular aspect of rotorcraft simulation—loosely joined for this purpose. This section will describe the two codes and how they work together to maximize simulation accuracy and efficiency.

CAMRAD II

CAMRAD II belongs to a family of software known as "Comprehensive Codes" for the analysis of rotorcraft. These analyses incorporate a myriad of models to simulate the different aeromechanical subsystems of rotorcraft. CAMRAD II brings together a multibody dynamics model, a nonlinear finite elements structural model, and an aerodynamics model based on lifting line theory [4]. CAMRAD II has seen a great deal of use in the simulation of the UH-60 aircraft in a variety of flight conditions [5–9].

The CAMRAD II structural dynamics model for the UH-60A has been decades in development by NASA and the U.S. Army. The specific model used here was refined by Yeo et al. in 2004 [10]. The model simulated the rotor using 7 1-D structural beam elements and 20 aerodynamic panels. The rotor was trimmed using Newton-Raphson iteration on collective and cyclic to meet specified trim targets.

OVERFLOW 2

All Navier-Stokes CFD analysis presented herein was performed using OVERFLOW 2 version 2.2b [11]. OVERFLOW 2 is an overset, structured-mesh flow solver developed at NASA. For two decades the OVERFLOW solver has served to analyze a variety of rotorcraft under a wide range of flight conditions [12]. OVERFLOW 2 offers a wide variety of numerical schemes, turbulence models, and boundary conditions. For the present study, OVER-FLOW 2 was run with 4th order central differencing and 4th order artificial dissipation in space. Time marching was performed using a 2nd order dual timestepping scheme. Turbulence was modeled near blade surfaces using the Spalart-Almaras one-equation model with rotational corrections. The turbulence model was deactivated in regions one chord length or further from the rotor blades to reduce numerical dissipation of the wake. Blade surfaces were modeled as viscous, adiabatic walls; outer boundaries were modeled using a characteristic condition imposing freestream quantities.

OVERFLOW 2 computes the flowfield by discretizing the Navier-Stokes equations on a series of overset, structured grids. Grids modeling the rotor blades were body-fitted and curvilinear. These grids, often called near-body grids, extended approximately one chord length from the blade surface. The near-body grids were nested within one or more grids, called off-body grids, which filled the space between the rotor and the boundary of the computational domain. The OVERFLOW 2 model included a notional hub, but the LRTA and wind tunnel struts were not modeled. All grids exchanged flow information in regions of overlap. The amount of this overlap was sufficient to support full 4th order accuracy at the boundaries.

The grid surface is the latest definition derived from the as-built CAD model. Notable differences between this surface definition and that of prior investigations [14,15] are an outboard shift of the trim tab by approximately 4 inches, a small bump on the upper surface near the blade grip, a slight thinning of the airfoil very near the tip, and a blunt trailing edge across the whole span.

The near-body grid representing the bulk of each rotor blade had an "O" topology with 157 points wrapping around the blade chordwise, 145 points along the blade span, and 75 points normal to the surface. The initial spacing at the blade surface had a y^{+} value of 1. This grid system is illustrated in Fig. 2. The baseline near-body grid system (the hub and all four blades) contained approximately 10.7 million points.

Two different off-body grid systems provided two different simulation scenarios:

The first system used a series of ever larger Cartesian grids to create shells expanding outward from the near-body grid set. The grid point spacing within each shell is twice that of the shell immediately preceding it. The finest off-body grid had a spacing equivalent to 0.1 tip-chord lengths in all three directions. Seven such shells created a cubic computational domain spanning ten rotor radii in every direction. Domain boundaries in this scenario were set to a freestream characteristic condition thereby simulating a rotor operating in free air. Flow in the off-body grids was treated as inviscid and the turbulence model was deactivated. This off-body grid set consisted of 15.5 million grid points and is depicted in Fig. 3.

The second off-body grid system used a single grid to envelop the near-body grid-set forming a computational domain that mimicked the size and shape of the wind tunnel test section. This grid made no attempt to model the contraction or expansion sections of the tunnel but rather maintained the test section profile for 4.6 rotor radii upstream and downstream. The rotor plane was located 20.4 feet above the simulated tunnel floor. The inlet end of the tunnel grid employed the same freestream characteristic boundary condition as the free air system, and the outlet plane used a boundary condition that ensured conservation of mass within the tunnel grid. Viscous terms of the Navier-Stokes equations were discarded for this grid. This paradigm was initially proposed by Chang et al. [16] This off-body grid contained 4.2 million grid points and is pictured in Fig. 4.

In addition, a refined version of the free-air grid system was prepared to ascertain grid convergence of the simulation. This grid system reduced grid point spacing in both the near-body and off-body, approximately doubling the number of grid points to 50.7 million.

Unless otherwise indicated, all predicted data presented herein were computed using the baseline near-body grid and the baseline free-air off-body grid set. This near-body and off-body combination totals 26.2 million grid points. To reduce computation time CFD simulations were run using a hybrid distributed/shared memory scheme with 160 Mes-
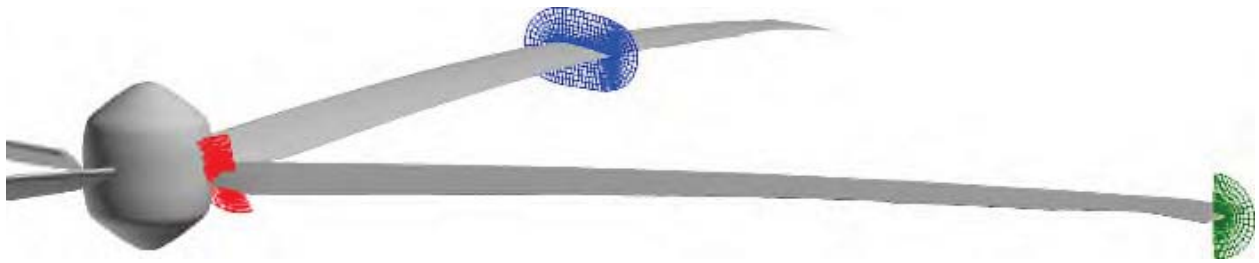
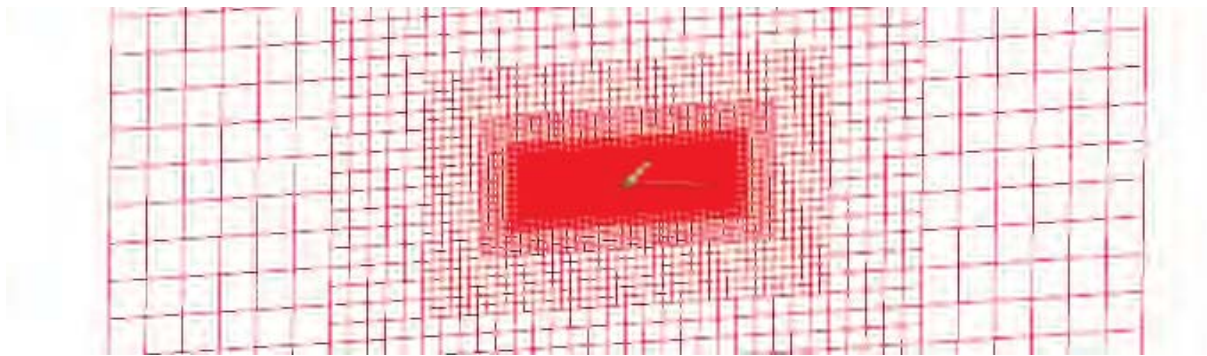**Figure 2** – OVERFLOW 2 Near-Body Grid System. (Not every point shown.)

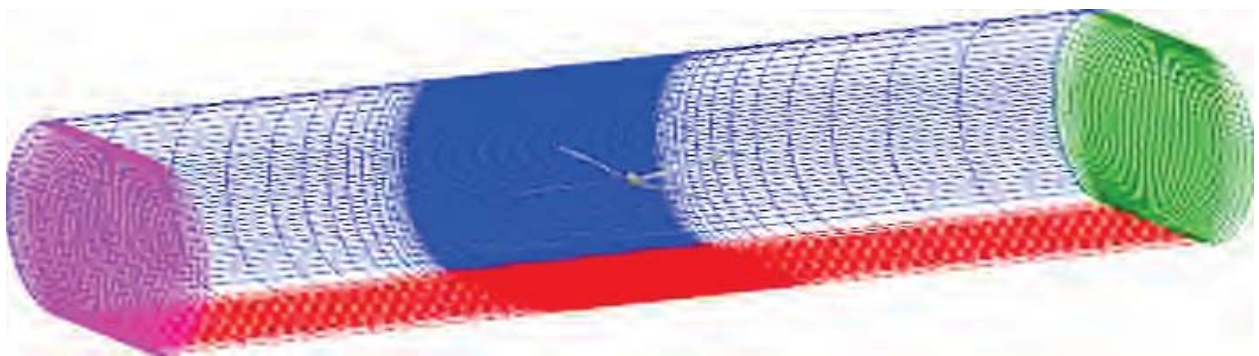**Figure 3** – OVERFLOW 2 Free-Air Off-Body Grid System.

Figure 4 – OVERFLOW 2 Wind Tunnel Off-Body Grid System. (Not every point shown.)

sage Passing Interface (distributed memory) ranks and eight OpenMP threads (shared memory) per MPI rank for a total of 1280 parallel tasks. OVER-FLOW 2 required approximately 31 minutes to advance the solution for this configuration ¼ of a rotor revolution using 1280 CPUs of an SGI Altix ICE computer.

Coupling Methodology

CAMRAD II uses a lower-fidelity aerodynamics model than that available in modern CFD codes, and most CFD codes lack the sophisticated Computational Structural Dynamics (CSD) and trim capabilities of comprehensive codes like CAMRAD II. Coupling a CFD code (e.g. OVERFLOW 2) to a comprehensive code (e.g. CAMRAD II) marries the strengths of the two approaches and produces the highest-fidelity solution currently possible. For this study, coupling is achieved by alternate execution of OVERFLOW 2 and CAMRAD II. At the end of each code's turn to execute, it passes data to the next code. The data passed from OVERFLOW 2 to CAMRAD II is airload data integrated from its Navier-Stokes model of the UH-60 rotor. This airload data is used to augment CAMRAD II's internal aerodynamics model (which consists of airfoil tables and a lower-order wake model). At the end of its execution, CAMRAD II generates updated control positions and a description of how the blade deforms elastically as it revolves around the shaft. These quantities are used to give OVERFLOW 2's grids a realistic motion in response to the aerodynamic environment. This algorithm, called the delta coupling technique, was pioneered by Tung et al. [13] and implemented in OVERFLOW by Potsdam et al. [14] Significantly improved airloads prediction capability has been demonstrated for the UH-60A rotor in steady level flight conditions using this loosely coupled approach [14, 15].

The CFD solution is advanced ¼ revolution during a coupling iteration because this allows each of the rotor's four blades to sweep through a full quadrant of the rotor disk. Taken in aggregate, the four blades thereby determine the airloads at every azimuth for every coupling iteration.

Convergence of the coupling process was determined by monitoring blade airloads for periodicity. When the airloads did not vary significantly from one coupling iteration to the next, the solution was judged to be converged. For the present analysis, this generally occurred after 24 coupling iterations. Since OVERFLOW 2 was allowed to iterate for ¼ revolution between coupling exchanges, this equates to 6 full revolutions for the converged solution. A fully converged coupled solution required approximately 17 hours to compute for the baseline grid on 1280 SGI Altix ICE processors.

Selected Test Conditions And Trim Approach

For the present investigation, two parametric sweeps were selected for analysis. First, a speed sweep was selected to test simulation accuracy over a wide range of advance ratios. Second, a thrust sweep was selected to test simulation accuracy under conditions ranging from a lightly loaded rotor through deep stall.

The selected speed sweep ranged from μ=0.15 to 0.4 with a constant C_L/σ=0.09 and a constant tip Mach number of 0.65. During testing, lift, propulsive force, and hub moments were trimmed to match nominal values at each flight condition by varying α_s along with collective and cyclic pitch. In CFD calculations it is difficult to change the shaft angle once it has been set, which complicates its use as a trim control in adjusting lift and propulsive force. Instead, these flight conditions were matched in simulation by setting a constant α_s as indicated by tunnel data while trimming C_T and hub moments to match tunnel values using collective and cyclic pitch.

The selected thrust sweep was conducted at μ=0.3 with M_{tip}=0.625, α_s=0°, and the rotor trimmed for minimum hub moments. The thrust was varied by changes in collective pitch up to stall. Absolute collective angles for a given thrust are generally different between simulation and test. To nullify this offset, a baseline case was selected at C_T/σ=0.08 and the simulation was trimmed to match the measured thrust. Collective deltas were derived from test data relative to this baseline and then applied to the simulated baseline to produce the remaining target points.

In all cases, free-air simulations used corrected shaft angles, α_c, derived from the geometric shaft angle, α_s, by applying a Prandtl-Glauert wall correction [1]. Simulations including tunnel walls used uncorrected shaft angle data.

Results

The 2010 UH-60A Airloads Test is a valuable resource not only for the breadth of flight conditions obtained but for the depth of detail available in each measurement. Failure of analysis to predict bulk loads accurately can be diagnosed by exploring detailed measurements and how they compare to quantities extracted from simulation results. This approach will now be applied to the present simulation methodology first for the selected speed sweep and then for the selected thrust sweep.

Speed Sweep

Integrated Results

Figure 5 plots the value of the trimmed thrust coefficient versus advance ratio for the range of speeds simulated. Since thrust was a trim target, it was expected that the computed points would lie very close to the measured data. Indeed this is the case for the data derived from CAMRAD II output. However, the data computed by integrating the pressure and viscous forces acting on the CFD grid yield a somewhat higher thrust. The average difference between the thrust reported by CAMRAD II and OVERFLOW 2 is 2.5%. There are a number of factors contributing to this difference. First, small discrepancies in the local twist between the OVERFLOW 2 model and the CAMRAD II model can alter the computed thrust by altering in-plane and out-of-plane contributions by normal and chord force. Second, the airloads passed from OVERFLOW 2 to CAMRAD II are only the loads integrated from the main blade grid and neglect any forces contributed by the tip and root caps. The coupling mechanism makes no effort to fully conserve forces between OVERFLOW 2 and CAMRAD II. Third, the CAMRAD II model used a low-resolution—just 20 aerodynamic panels spanwise and 24 azimuthal stations—representation of the rotor disk. This low-fidelity representation doubtlessly fails to capture all of the nuances of the spanwise loading on the blade. CAMRAD II is capable of including many more aerodynamic panels in its blade model, and doing so should henceforth be considered standard practice. Improving force conservation in the coupling process is an area that requires future work.

Since the OVERFLOW 2 model contains the most complete representation of the rotor aero-
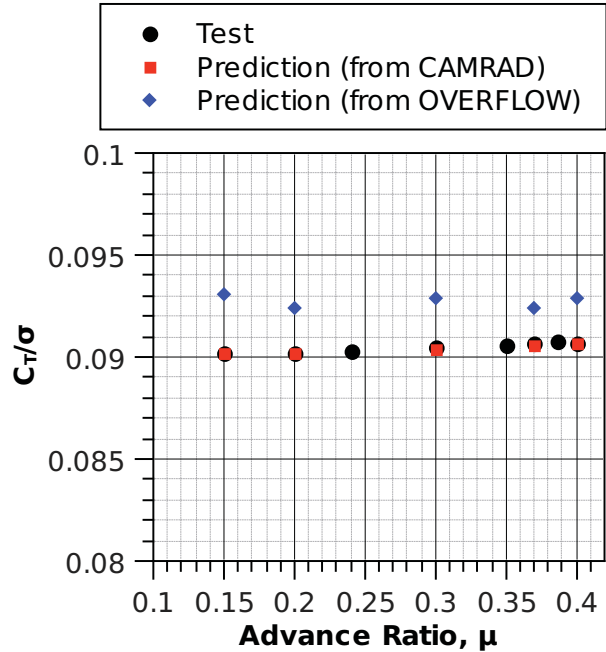

Figure 5 – Thrust Trim for Speed Sweep.

dynamics, only its data will be presented in the remainder of this paper. The reader should bear in mind that all results presented here are the result of a trim solution with a slightly higher ($\sim$2.5%) than prescribed thrust.

Recall that the CFD calculations for the speed sweep were performed by matching the wall corrected shaft angles from the test data rather than trimming propulsive force. Figure 6a shows the difference between corrected and uncorrected shaft angle as a function of advance ratio. Figure 6b depicts the corresponding propulsive force at each speed. Propulsive force is underpredicted at low speed and overpredicted at high speed. A portion of this prediction error at high speed is due to inaccurate trim. The large shaft angles at high speed divert a substantial portion of the excess thrust due to trim error into propulsive force.

Figure 7 compares measured and predicted power. Figure 7a shows total power which is underpredicted by approximately 2%. Figure 7b is formed by removing the parasite power from Fig. 7a leaving the sum of profile and induced power, the two of which are inseparable in CFD simulation. From Fig. 7b it is clear that the simulation is having difficulty predicting profile and induced power accurately at the high speed points. This is masked in Fig. 7a by a fortuitous overpredic-
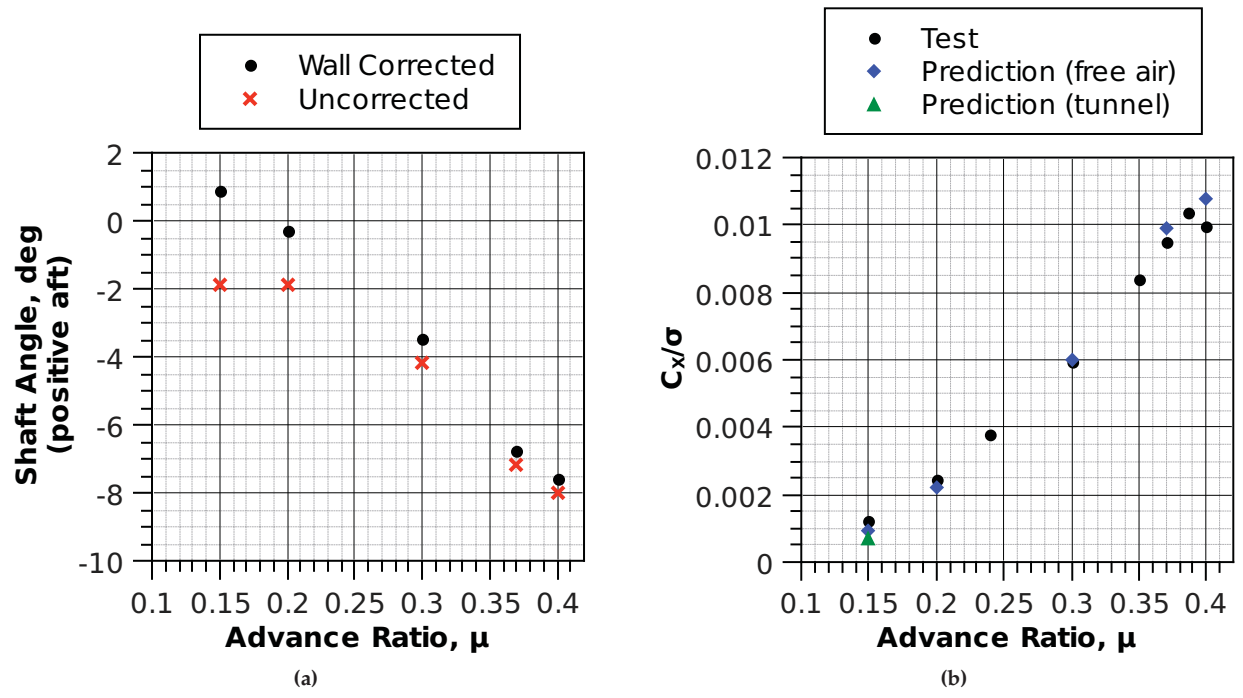
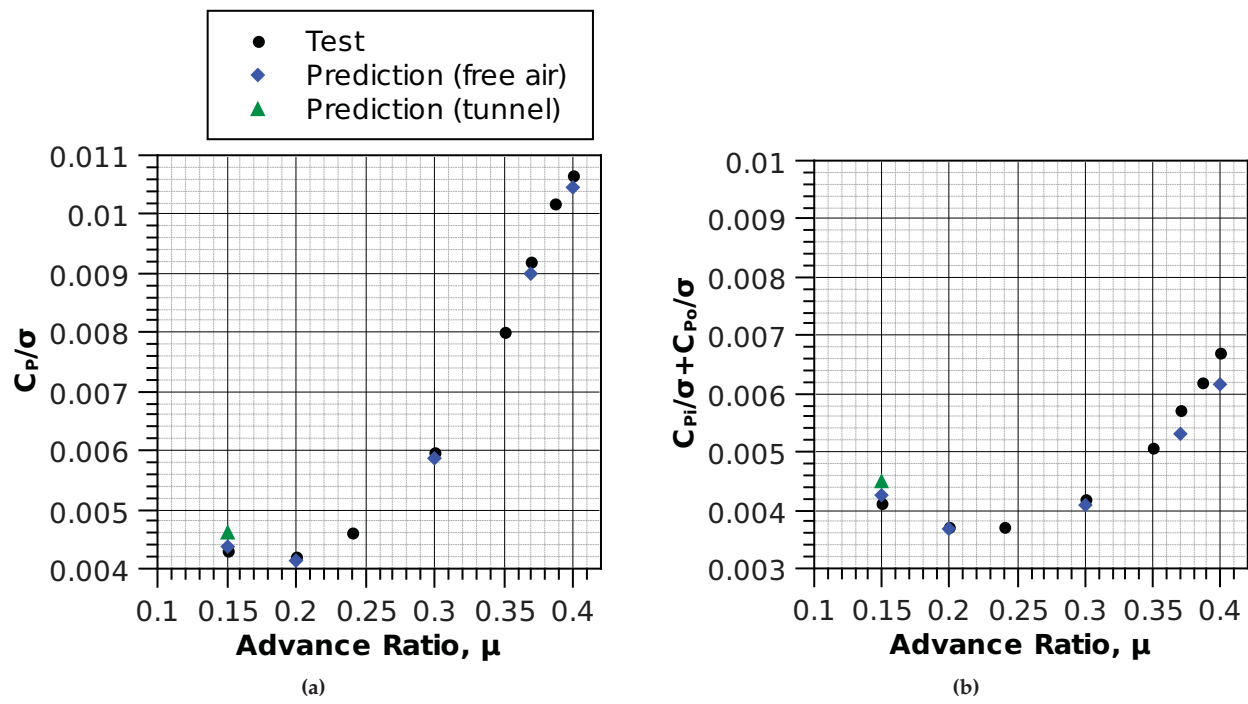**Figure 6** – Prescribed Shaft Angle and Resultant Propulsive Force for Speed Sweep.

Figure 7 – Speed Sweep Power.

tion of propulsive force, and hence parasite power, at these points. A more accurate trim would result in a small thrust reduction, causing a complementary reduction in induced power, further degrading the correlation throughout Fig. 7 slightly.

Also shown in Figs. 6 and 7 are predictions using the simulated tunnel walls for a single condition (μ=0.15). The C_x data from this model has been corrected using the same Prandtl-Glauert wall correction used for the test data and is included in Fig. 6b. Predictions with the tunnel walls underpredict propulsive force and overpredict power at this advance ratio to a greater extent than free air simulations. One possibility is that the inviscid walls of the simulation necessitate a different wall correction than the test measured data.

Sectional Comparisons

In Fig. 8 are presented the sectional loads—M^2c_n, M^2c_m, M^2c_c—at several radial stations for the lowest speed in the speed sweep, μ=0.15. All data are presented with means included. This is at a slightly higher thrust than, but otherwise is similar to, the oft-studied c8513 flight condition from the UH-60 flight test [3, 14].

Several predicted curves are plotted against the test data. The first, in green, was computed using the 26.2 million point baseline grid. The second was computed with the 50.7 million point fine grid, in red. Although there are instances where the fine grid improves on the baseline solution (e.g. M^2c_c on the advancing side at $^r/_R$=0.865), there are also instances where the solution on the baseline grid is closer to the measured data (e.g. M^2c_m in the second quadrant at $^r/_R$=0.92). Otherwise, these two curves are very much in agreement with each other. Because the baseline grid performed so well for this low-speed flight condition—where accurate capture of the wake is most important—it was decided to use the baseline grid for the remainder of this study.

In general, the trends in normal force are well matched. The normal force pulses due to blade vortex interaction (BVI) begin to appear at $^r/_R$=0.775 on both the advancing side (near ψ=70°) and retreating side (near ψ=280°). These BVI events are visible in the CFD wake visualization of Fig. 9. The magnitudes of the normal force pulses in Fig. 8 are accurately captured by the simulation save for a small underprediction on the advancing side BVI at $^r/_R$=0.865. The largest missed predictions are

mean shifts at $^r/_R$=0.4 and 0.865. In addition, a small surge in normal force from ψ=120° to 180° is present in the test data for all of the outboard stations, but the analysis prefers a nearly continuous decrease in normal force throughout the second quadrant.

The pitching moment is generally mean shifted with a tendency toward overprediction. It should be noted that the pitching moment measured during the test is very sensitive to transducer performance at the trailing edge, so a mean shift is likely to include significant measurement error. One common exception to the trend of overpredicted mean occurs at $^r/_R$=0.775. A possible cause is the trim tab which extends from $^r/_R$=0.73 to 0.86. The trim tab on the tested blades was deflected upward by approximately 2° which increases the local pitching moment significantly compared to adjacent stations. Although the trim tab is represented in the CFD grid, it is not deflected, and the predicted pitching moment mean changes little compared to $^r/_R$=0.4 or 0.865. The moment pulses due to BVI are predicted accurately in phase but the peak-to-peak amplitude is generally smaller compared to measured data.

Chord force displays a significant mean shift with a tendency toward underprediction. There is an additional offset that further reduces the chord force only on the advancing side. The sign convention for chord force is positive toward the leading edge so an underprediction represents an excess of drag. One contributor to this disparity between measurement and prediction is viscous force. The test data is derived from integrated pressure measurements with no correction for viscous effects, while the predicted data is the combination of integrated pressure data and viscous drag at the airfoil surface. Predicted airloads computed from pressure data alone are also presented in Fig. 8. Note that the viscous forces make significant contributions solely to chord force, and that they make the largest contribution on the advancing side near the tip. However, the viscous forces account for at best 20–30% of the difference between measurement and prediction. Despite the mean shift, the trend in chord force is well represented. Drag excursions coincident with the BVI events are captured by analysis, particularly on the retreating side where the measured drag pulse is closely matched in magnitude, phase, and shape.
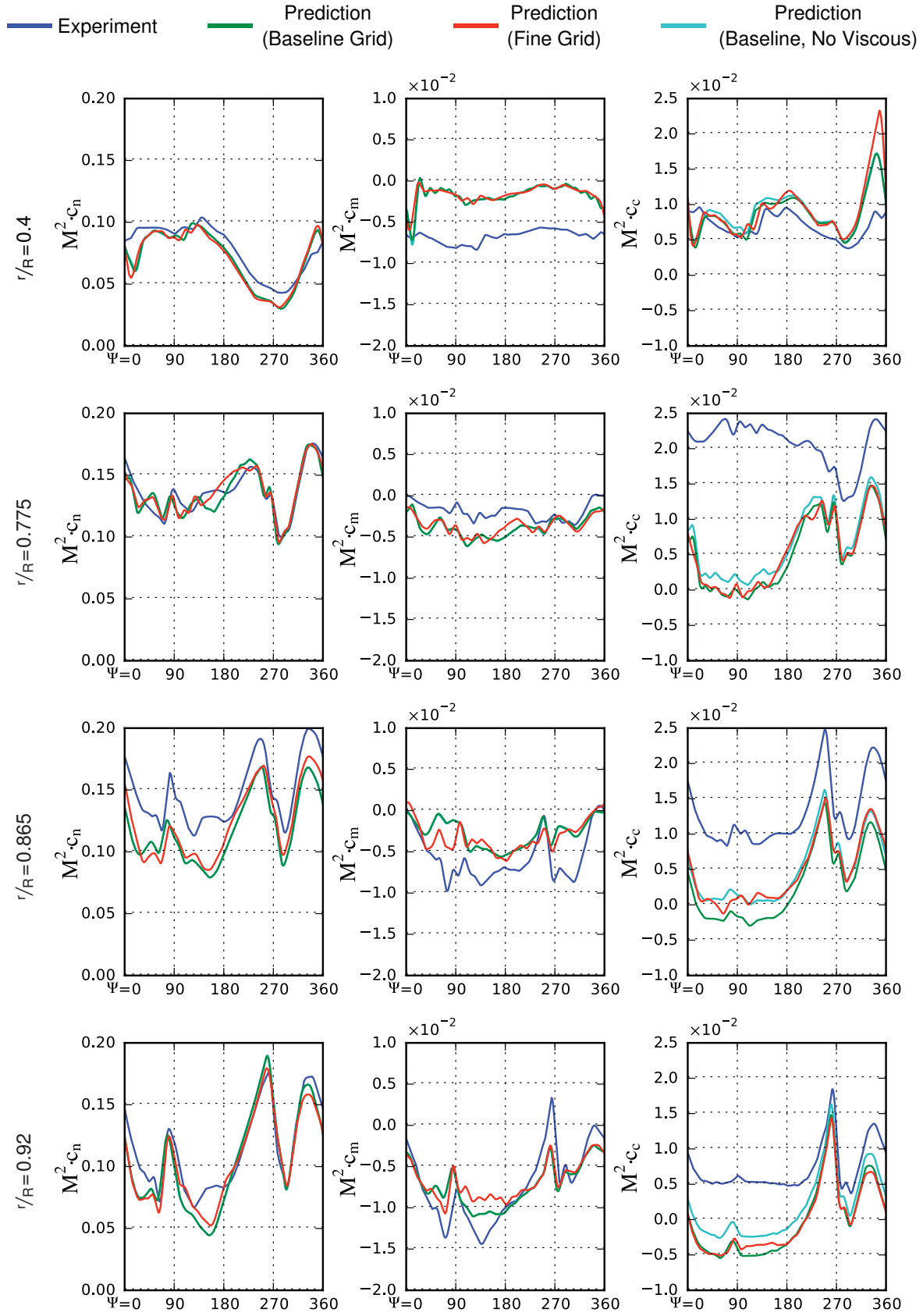
Figure 10 contains the same measured and

Figure 8 – Sectional Airloads at $\mu=0.15$, $C_T/\sigma=0.093$.
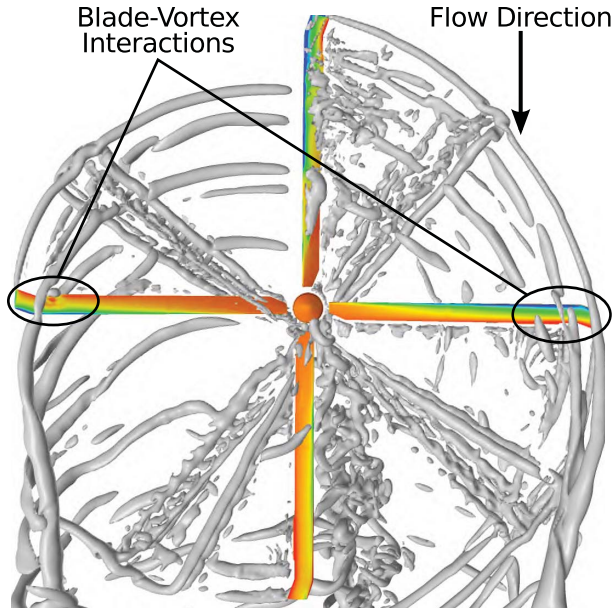
Blade-Vortex Interactions

Flow Direction

Figure 9 – Wake Visualization From CFD. Isosurface of Q-Criterion With Blades Colored By Pressure.

free-air predicted data from Fig. 8 but compares it to data predicted using the tunnel wall model. The largest differences between the free-air model and the tunnel model appear on the advancing side, particularly near the $\psi=90°$ BVI. This event appears slightly attenuated compared to the free-air model in all three coefficients and at all of the stations where it is to be observed.

The low speed case is when the tunnel walls exert their maximal effect on rotor performance. Yet the free-air simulation compares well to the corrected test and tunnel simulation data for both integrated and sectional loads. This suggests that the simple Prandtl-Glauert correction for angle of attack is reasonable.

Figure 11 presents the sectional airloads at the highest advance ratio in the speed sweep, $\mu=0.4$. At the two outboard stations the analysis predicts a dynamic stall cycle in the fourth quadrant. This is identifiable as dips in all three coefficients just after $\psi=270°$. Although there is some evidence of stall in the test data (particularly in chord force), the magnitude of the stall event was predicted to be much larger than was measured. The normal force trend is well represented, except for a tendency to overpredict the negative lift on the advancing side. Pitching moment predictions show larger differences. From $r/R=0.775$ outboard, a mo-

ment pulse due to supercritical flow appears on the advancing side at $\psi=90°$, but its magnitude is diminished in prediction. For both of the outboard stations, the analysis underpredicts the magnitude of the moment on the advancing side. Chord force results are well correlated at the inboard station, $r/R=0.4$. At $r/R=0.775$ the chord force trend on the advancing side is completely missed, but this may be an effect of the difference in trim tab deflection. At the two outboard stations, chord force remains underpredicted on the advancing side, but the shape of the predicted chord force curve follows that of the test for the first two quadrants, even replicating the two small peaks in the second quadrant. Differences in the fourth quadrant are consistent with excessive stall in the simulation.

Figure 12 presents a side-by-side comparison of test and predicted normal force coefficient at $r/R=0.92$ for every speed in the sweep for which a simulation was run. The test data exhibits vortex induced loading at $\psi=70°$ and $280°$ for the lowest advance ratios. At higher advance ratios, the increasingly negative loading in the second quadrant balances increased normal force over the rest of the rotor disk. The second quadrant minimum starts at approximately $\psi=135°$ and draws toward $\psi=90°$ as advance ratio increases.

Figure 13 makes the same comparison as Fig. 12 but for moment coefficient. In the test data, vortex effects are again evident at the lowest advance ratios near $\psi=70°$ and $280°$. A large moment pulse consistent with supercritical flow develops near $\psi=80°$ for the highest advance ratios. The moment minimum in the second quadrant migrates from $\psi=135°$ at $\mu=0.15$, toward $\psi=90°$ at $\mu=0.3$, and then back to $135°$ by $\mu=0.4$. Lastly, the test data appears to exhibit a weak stall event near $\psi=315°$ at $\mu=0.4$.

Observing the evolution of the advancing side normal force trough in Fig. 12 reveals that both the test and analysis display the same monotonic reduction in normal force with speed. The change in minimum normal force from one speed to the next appears slightly larger for the prediction than in test. The simulation also predicts significant lift loss from stall in the fourth quadrant at the two highest speeds. No corresponding feature is present in the measured data. Despite the differences in moment coefficient magnitude between test and prediction in Fig. 13, the trend between speeds is very similar. The advancing side shock grows in strength
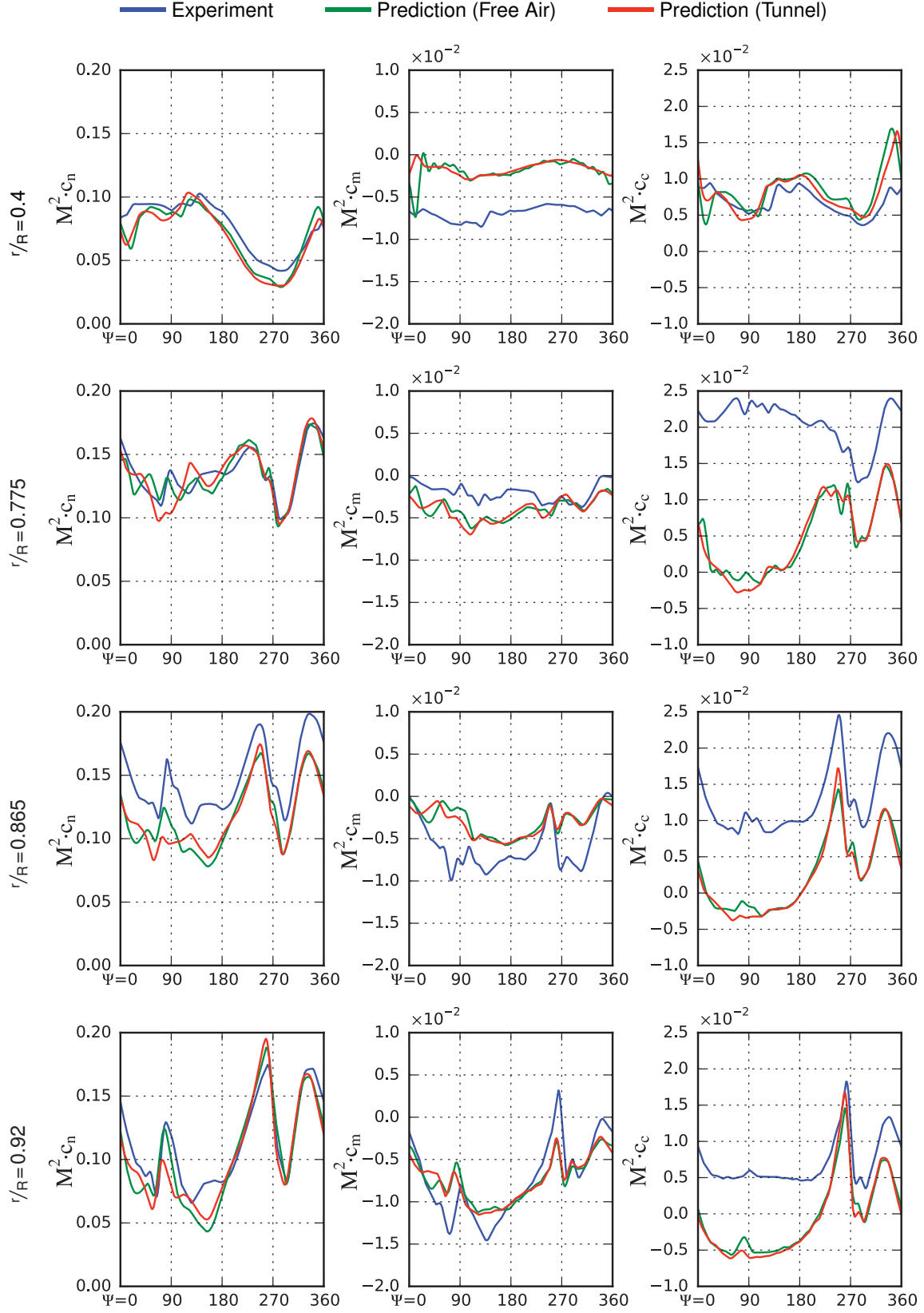
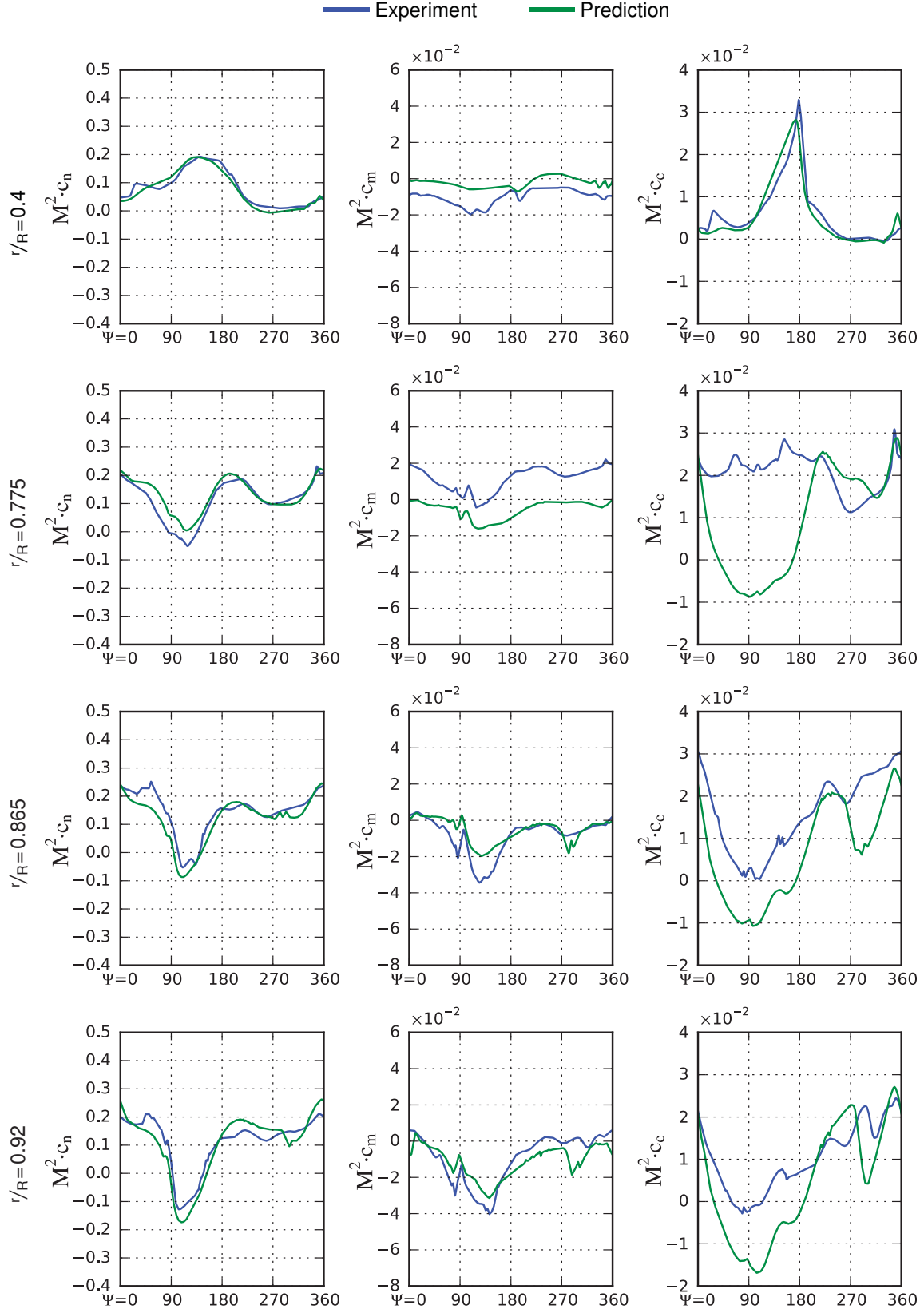**Figure 10** – Sectional Airloads at μ=0.15, C_T/σ=0.093. Free Air Vs. Tunnel Model.

Figure 11 – Sectional Airloads at μ=0.4, C_T/σ=0.093.
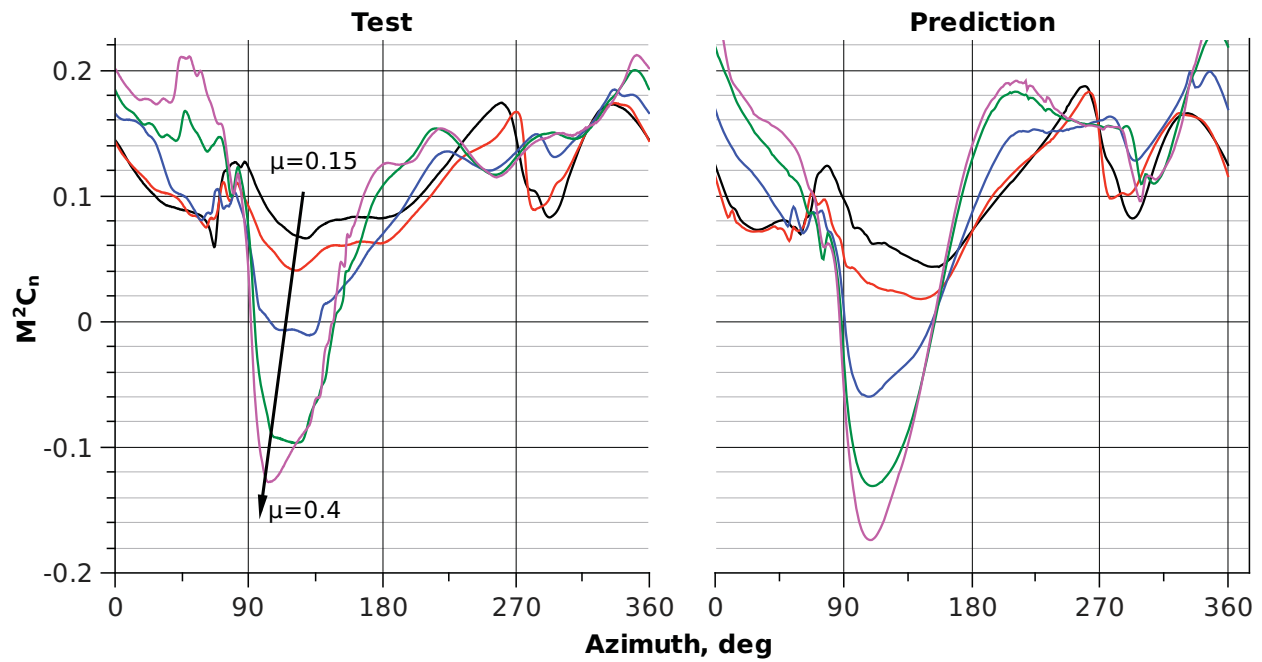
Figure 12 – Normal Force Coefficient at $^r/_R$=0.92 for μ=0.15, 0.2, 0.3, 0.37, 0.4. C_T/σ=0.093.
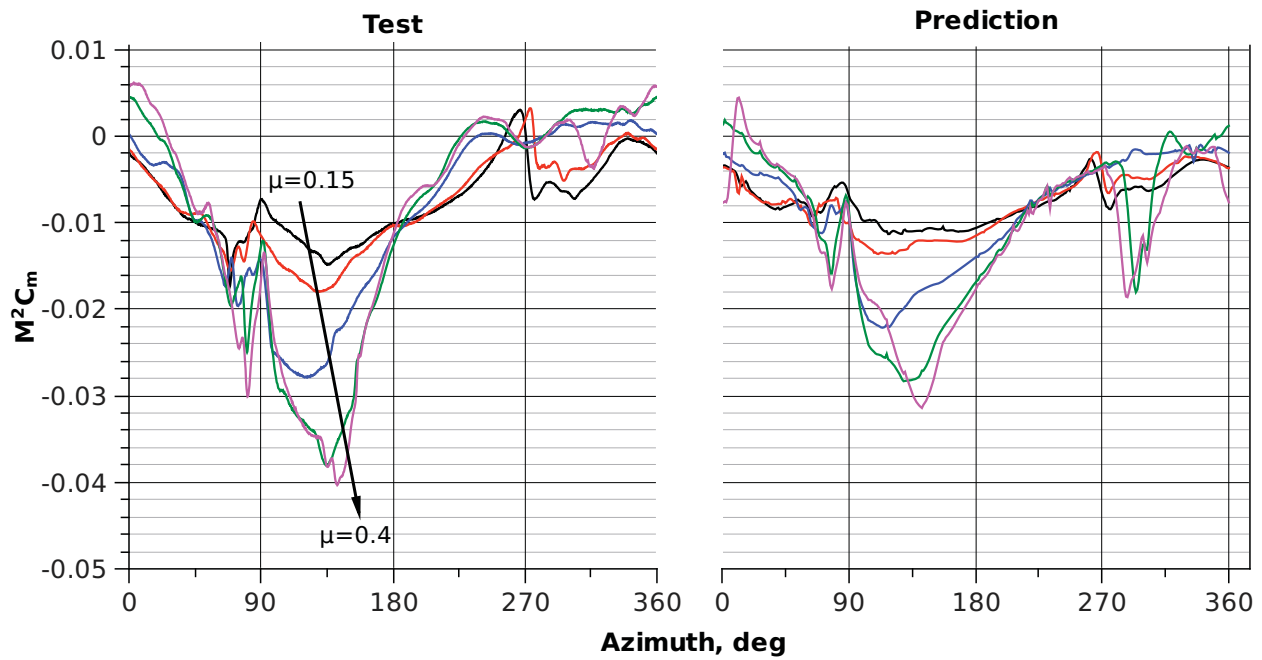

Figure 13 – Moment Coefficient at $^r/_R$=0.92 for μ=0.15, 0.2, 0.3, 0.37, 0.4. C_T/σ=0.093.

and migrates toward $\psi=90°$. The moment trough behind the shock also evolves very similarly across the speed range. Differences include an expansion of the trough into the third quadrant for the predicted data, the prediction of a stall cycle at $\mu=0.37$ when none is present in measured data, and an enhancement of the predicted stall cycle at $\mu=0.4$ compared to measurement.

Thrust Sweep

Integrated Results

Presented in Fig. 14 are the predicted performance results for the selected thrust sweep. From this figure it is clear that the analysis performs well at predicting the maximum rotor thrust and the relationship between power and thrust throughout the sweep. Recall that the analysis was trimmed to match thrust at the $C_T/\sigma=0.08$ point but that in general CFD integrated thrust is slightly higher than specified. This leads to a small thrust surplus throughout the linear region since all collective angles are set relative to the baseline condition. At high collectives the excess thrust vanishes because the rotor is stalled and appears incapable of producing more thrust. The analysis also exhibits reduced sensitivity to collective change evidenced by an approximately 7% reduction of slope in the linear region.

Power is generally overpredicted, with differences up to 11% at the highest thrust conditions (Fig. 14b). The fact that the predicted and measured points lie on very similar curves, however, suggests that if thrust was rigorously matched, power may be better predicted.

Sectional Comparisons

Sectional airloads for the minimum collective setting are presented in Fig. 15. At this collective, the measured thrust was $C_T/\sigma=0.02$. The normal force bucket in the second quadrant is narrower and shallower in prediction than in test. Normal force is also slightly overpredicted for the majority of the retreating side, except at the inboard station. Moment coefficient mean is well predicted at this condition—except at $r/R=0.4$—but there exist significant differences in trends between analysis and test. For example, there is a shock-induced moment pulse that appears in the second quadrant at $r/R=0.775$, migrates toward the first quadrant,

and ends in an interesting double pulse at $r/R=0.92$. Although the phase of these pulses is well correlated, the peak-to-peak magnitude of the predicted pulses is smaller. Moment recovery following the shocks also begins too early and progresses slowly compared to measurement for $r/R=0.865$ and 0.92. Chord force continues to be mean shifted outboard of $r/R=0.775$, and the trend is completely mispredicted at $r/R=0.775$.

The sectional airloads presented in Fig. 16 are for the maximum collective condition where $C_T/\sigma=0.1255$. Comparisons at this condition must be tempered with the knowledge that stall is by nature a chaotic phenomena and there exists considerable variation in loading from one revolution to another, even in simulation. Test data in Fig. 16 are average loads sampled from 128 revolutions, but computing an ensemble average from CFD is impractical. The predicted data provided in Fig. 16 are instead single-revolution snapshots.

The flow at the inboard station remains relatively benign and correlation is good. The most significant deviations are a familiar mean shift in pitching moment and a blunting of the chord force peak in the second quadrant. Outboard, the loading is dominated by two severe stall cycles clearly indicated near the forth quadrant. The analysis appears to phase shift the stall cycles slightly, predicting both events perhaps 15° earlier than measured in test. Despite the phase shift, the magnitudes of the stall events are well predicted. One glaring difference at this deeply stalled condition is a large first-quadrant excursion in all three coefficients for the prediction. The similarity between the frequency of this event and the torsional mode of the blade suggests that it is a torsional response to the fourth quadrant stall cycles.

Figure 17 compares sectional normal force at $r/R=0.92$ for all collective settings simulated. The experiment observed an interesting evolution of normal force in the second quadrant. The normal force increased with collective until $C_T/\sigma=0.12$ after which it began to decrease, forming a narrow trough at approximately $\psi=120°$. The normal force reduction beginning at $C_T/\sigma=0.12$ is necessary to maintain roll balance across the rotor. Also visible in the test data is the development of two stall cycles, one at $\psi=290°$ and the second at $340°$.

Figure 18 presents moment coefficient at $r/R=0.92$ for all collective settings simulated. The most prominent features in the test data are the two
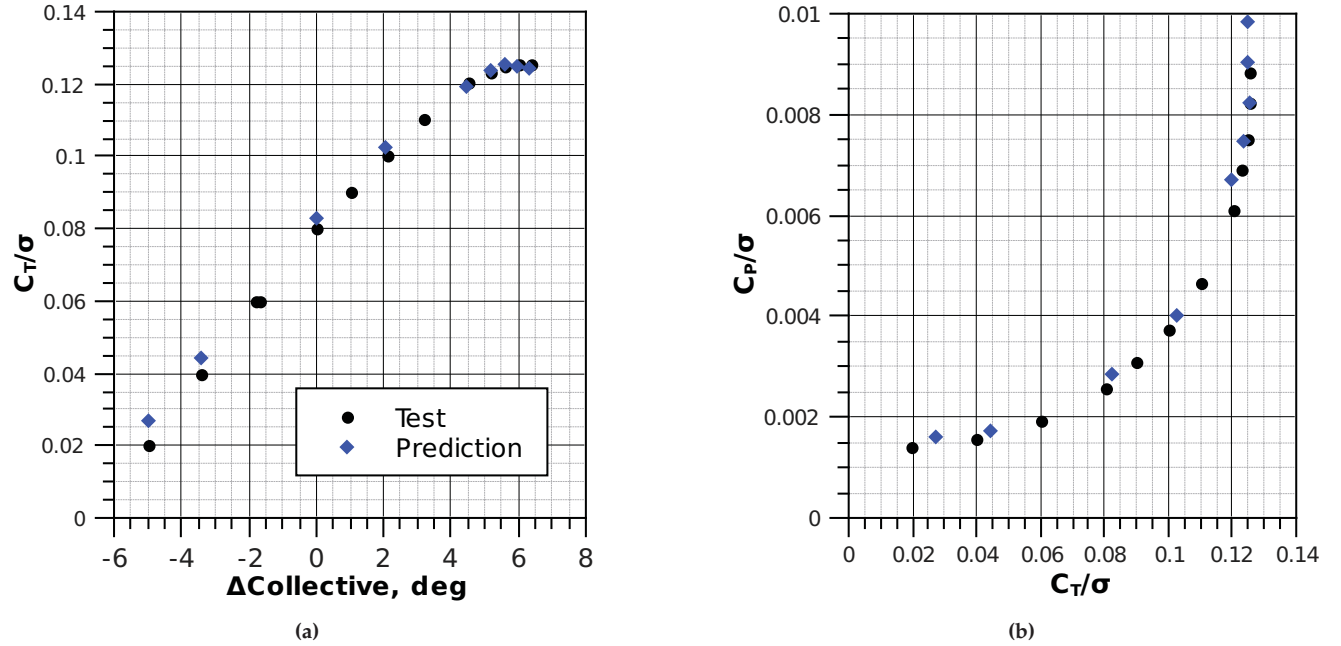
Figure 14 – Integrated Performance Results for Collective Sweep. $\mu = 0.3$, $M_{tip} = 0.625$, $\alpha_s = 0°$.

moment stall events that develop in the fourth quadrant. Both stall cycles appear abruptly at $C_T/\sigma = 0.12$. The first stall cycle quickly achieves a stable minimum moment which slowly drifts toward $\psi = 270°$. This is in contrast to the second stall cycle where the moment decreases rapidly and monotonically but remains fixed in azimuth.

Changes in normal force from one collective setting to the next are similar between test and prediction, with only a few notable differences. Foremost are the advancing side oscillations in the predicted data. This oscillation begins abruptly at $C_T/\sigma = 0.120$ and increases in magnitude along with collective. Examining the predicted moment coefficient data in Fig. 18 reveals that there is a single weak stall event at $C_T/\sigma = 0.10$ which quickly strengthens and spawns a second stall event by $C_T/\sigma = 0.120$. This suggests that the advancing side oscillation present in the predicted data is a response to either the strengthening of the first stall event, the formation of the second stall event, or both. Figure 19 plots the local pitch angle at $r/R = 0.92$ for three of the highest collective settings. At $C_T/\sigma = 0.10$ the rotor has a single stall cycle and very little torsional oscillation is visible in Fig. 19. As thrust increases, the fourth quadrant stall cycles strengthen concurrently with a 5/rev torsional oscillation in Fig. 19. This 5/rev oscillation grows

in magnitude and ultimately persists through all four quadrants at $C_T/\sigma = 0.1255$. Another difference is the second quadrant negative loading in Fig. 17 which is distorted in the predicted data. The trough is diminished in magnitude and shifted toward the end of the second quadrant. This difference appears to be a consequence of the torsional oscillation persisting into the second quadrant.

The effects of the torsional oscillation are also readily visible in the predicted data for Fig. 18. The oscillation dominates the predicted data in the first quadrant for the high thrust cases. The oscillation may also be responsible for the missed prediction of the moment minimum appearing in the test data at $\psi = 135°$. Examine the stall cycles in the fourth quadrant. The predicted responses are more chaotic and appear to have higher frequency content than the measured data. The first cycle marches toward 270° in an orderly fashion according to test data, but the analysis predicts a wider azimuthal range for the minima and high-frequency oscillations make it difficult to discern any orderly progression. The final location of the first stall cycle—at $C_T/\sigma = 0.1255$—is very similar between test and prediction. Comparisons between test and prediction for the second stall cycle include many of the same observations. The high frequency content of the predicted data make it
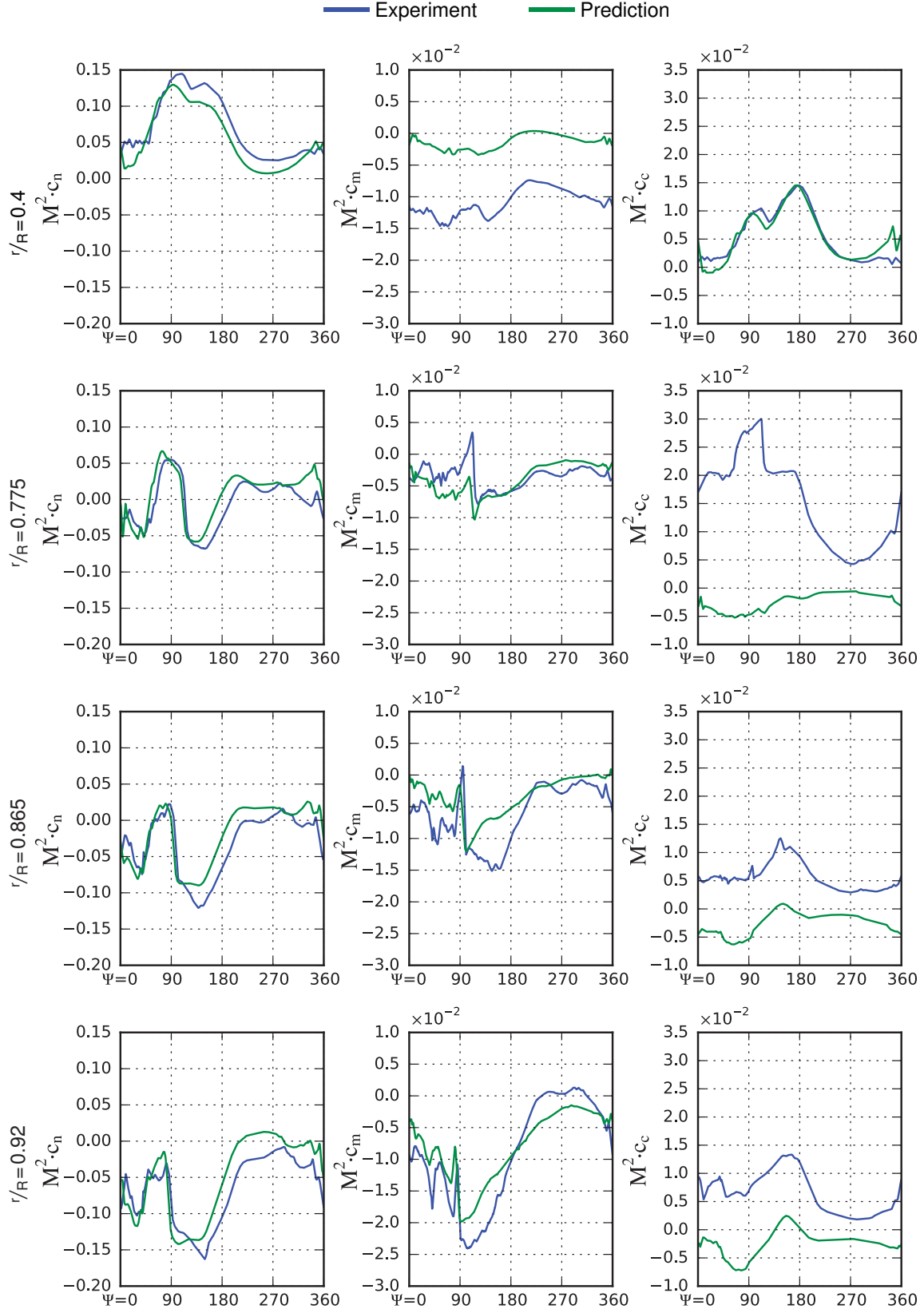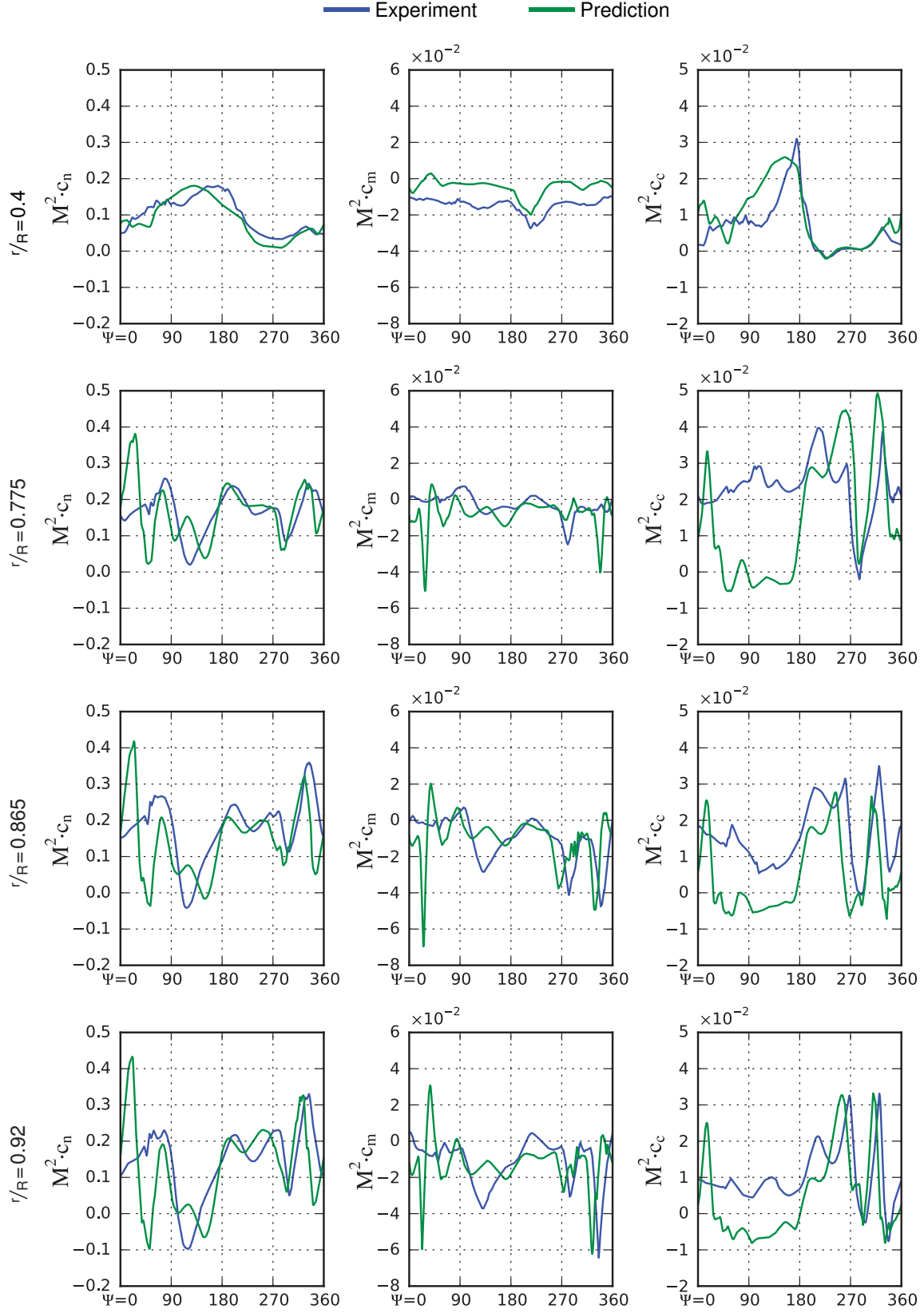
15

Figure 15 – Sectional Airloads, $C_T/\sigma = 0.02$.

Figure 16 – Sectional Airloads, $C_T/\sigma = 0.1255$.

Figure 17 – Normal Force Coefficient at $r/R = 0.92$ for $C_T/\sigma = 0.02$, 0.04, 0.08, 0.10, 0.120, 0.123, 0.1247, 0.1253, 0.1255. (Measured values, predicted C_T/σ is slightly higher.)
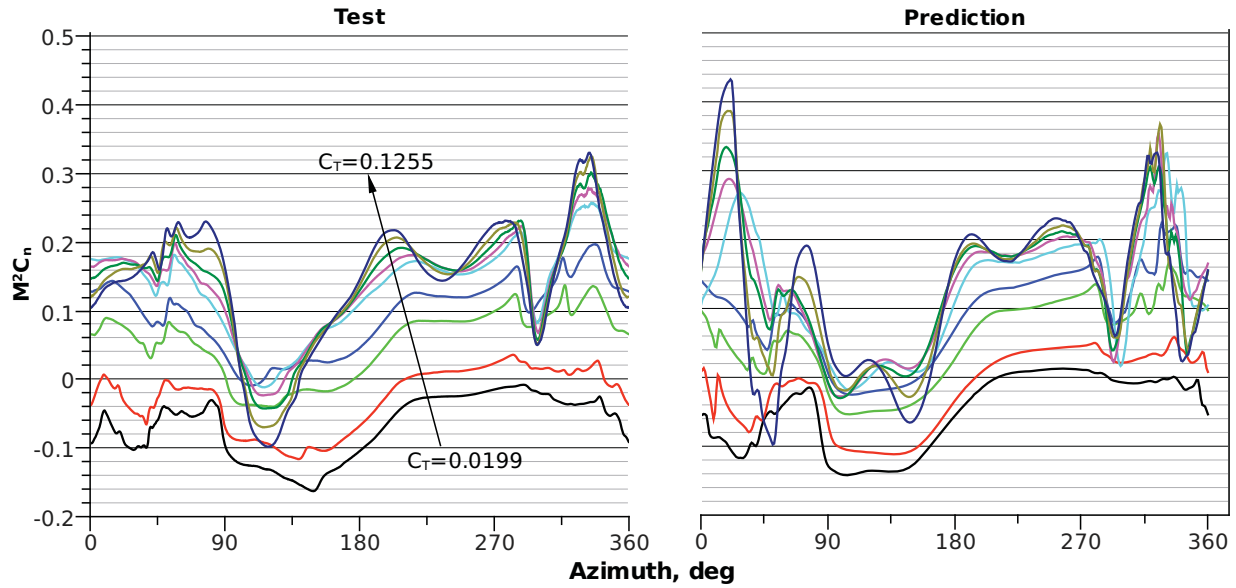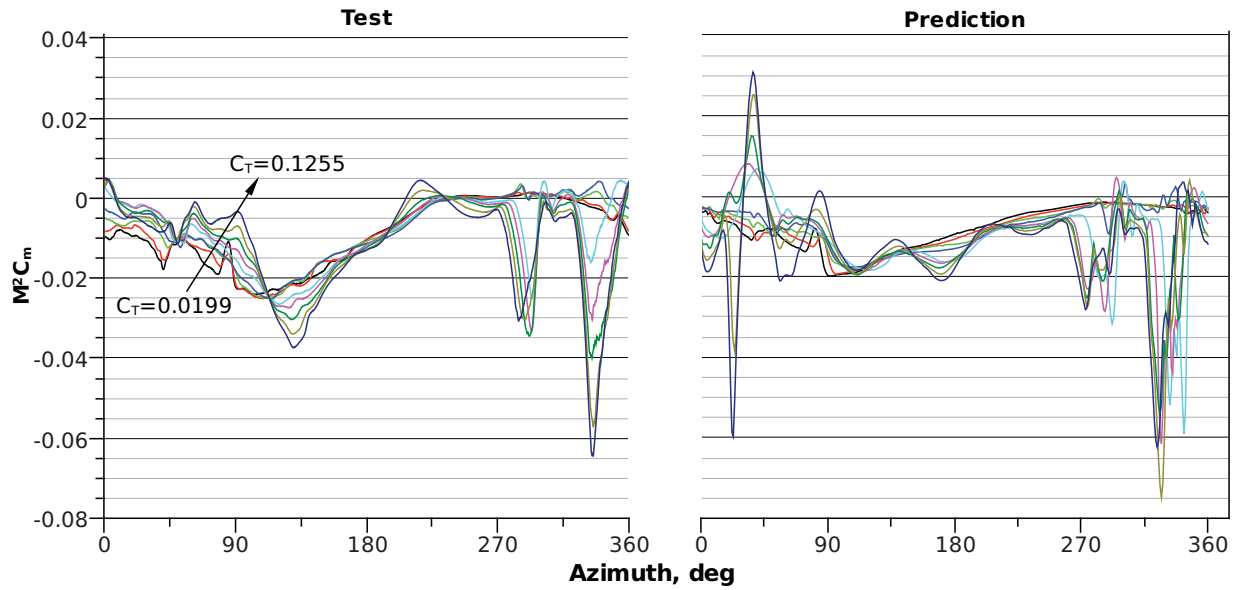

Figure 18 – Moment Coefficient at $r/R = 0.92$ for $C_T/\sigma = 0.02$, 0.04, 0.08, 0.10, 0.120, 0.123, 0.1247, 0.1253, 0.1255. (Measured values, predicted C_T/σ is slightly higher.)
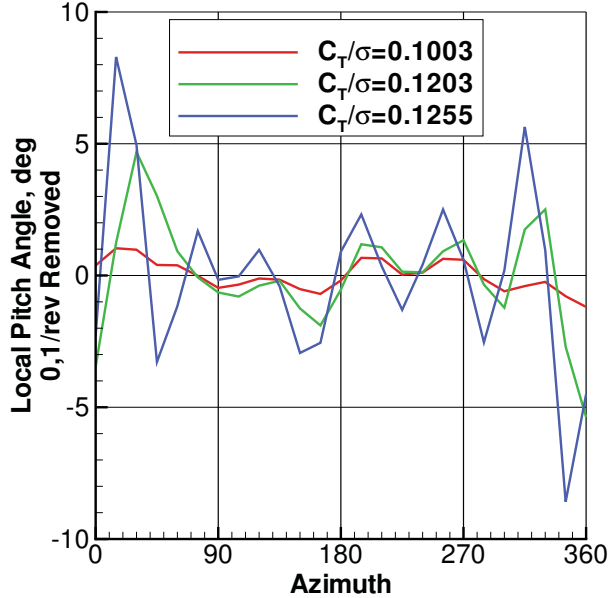
Figure 19 – Local Pitch Angle at $^r/_R$=0.92, $^2/_{rev}$ and Above.

difficult to accurately locate the minimum, but the majority seem clustered near 320°. The test shows a slightly later location for the second stall cycle, around 330°.

Conclusions

This paper has described the initial effort to correlate prediction with wind tunnel measurements from the recently completed UH-60A Airloads wind tunnel test. Differences identified in the present work represent opportunities to improve prediction methodologies or identify defects in measured data.

The simulation methodology involved a comprehensive rotorcraft simulation package, CAMRAD II, augmented with the first-principles aerodynamics of a CFD simulation provided by OVERFLOW 2.

Two parametric sweeps from the wind tunnel test were modeled: a speed sweep at constant lift and a thrust sweep at constant speed. Simulation of both sweeps were complicated by a disagreement between the two simulation codes on the integrated trim targets. The largest effect of this disagreement is a discrepancy of 2.5% in the trimmed thrust between the two codes, with the CFD being the higher of the two. Because they are a more complete rep-

resentation of the aerodynamics, only loads from CFD have been used for the present work. Further work is required to improve the coupling mechanism and CAMRAD II model to minimize discrepancies in loading between the two codes.

For the speed sweep, the analysis displayed a tendency to underpredict propulsive force at low speed and overpredict it at high speed. This may be partially attributable to inaccurate trim. The analysis underpredicted total power by approximately 2%. Although total power appears to be consistently predicted across the speed range, at high speed it is just a fortunate result of compensating errors—overpredicted parasite power on one side with underpredicted profile and induced power on the other. When applied to the thrust sweep, the analysis was very accurate at predicting maximum thrust and at capturing the relationship between thrust and power. Before the rotor stalled, there was a small increase in thrust attributable to inaccurate trim in the simulation at the baseline condition. The predicted thrust also exhibited a reduced sensitivity to collective pitch resulting in a shallowing of the slope in the thrust vs. collective curve. Power was consistently overpredicted—as much as 11% at the peak of stall. However, the variation of power with thrust is very similar between simulation and test. This suggests that power may be better predicted if the simulation trim were more accurate.

Detailed sectional loading comparisons reveal a number of differences between measurement and prediction. In general, correlation of normal force was good, with the prediction only occasionally deviating from test measurement. Comparisons of pitching moment exhibited more variation. Pitching moment predictions were frequently offset from measurement. It was noted that these comparisons are hampered by the difficulty of accurately measuring the mean pitching moment in test. Noteworthy flow features such as blade-vortex interaction, supercritical flow, and stall are accurately located in azimuth but the predicted magnitude of these events is often diminished. Chord force predictions bore the least resemblance to test data. These comparisons were often characterized by mean shifts and a large overprediction of drag on the advancing side of the rotor. As much as 20–30% of this difference is attributable to viscous forces included in predictions but absent from test data. Correlation of all three sectional coefficients at $^r/_R$=0.775

may be improved by correctly modeling trim tab deflection.

Other observed trends included a tendency for the analysis to overpredict the severity of stall, frequently predicting it at lower advance ratio and further inboard on the blade than indicated by measurement. Individual stall events are not as well defined in prediction as in test and their azimuthal locations do not progress smoothly as thrust increases. Also, for flows exhibiting a shock at or near $\psi=90°$, the moment trough that formed in the second quadrant just after the shock generally extended into the third quadrant according to simulation, but the corresponding feature was confined to the second quadrant in the test.

One final observation was made only for the deeply stalled cases of the thrust sweep. The analysis predicted a large oscillation in all three sectional coefficients beginning in the first quadrant and persisting into the second. No such excursion was present in the measured data. This has been shown to be a torsional response of the blade model to the formation of stall cycles in the fourth quadrant.

Modeling wind tunnel walls in the CFD simulation made only small differences in the sectional loads at $\mu=0.15$. The largest differences were on the advancing side near the $\psi=90°$ BVI. Larger differences were observed in the integrated performance parameters, with the free-air model outperforming the tunnel model. Further work is required to determine if this is a trend or merely an isolated misprediction.

The goal of this work was to provide an initial correlation with the newest data from the U.S. Army/NASA UH-60 test program. This dataset is of tremendous value to the rotorcraft community for the breadth of flight conditions sampled and the variety of detailed measurements made at each. No significant anomalies were identified in the test data studied, but the correlation effort revealed a number of areas for improvement in the simulation technique. Development is required to improve the coupling mechanics between CAMRAD II and OVERFLOW 2. Better force transfer between the two is mandatory for improving trim accuracy and accurately predicting integrated loads. Accurate power prediction remains a challenge for analysis. More detailed investigation is necessary to identify the cause of the stall-related torsional oscillation in the blade model and to improve the capture of sectional loading details such as dynamic stall and the effects of supercritical flow.

References

[1] Norman, T.R., Shinoda, P., Peterson, R.L., and Datta, A., "Full-Scale Wind Tunnel Test of the UH-60A Airloads Rotor", American Helicopter Society 67th Annual Forum, May 2011.

[2] Lorber, P.F., "Aerodynamic Results of a Pressure-Instrumented Model Rotor Test at the DNW", *Journal of the American Helicopter Society*, Vol. 36, No. 4, October 1991.

[3] Kufeld, R.M., Balough, D.L., Cross, J.L., et al., "Flight Testing of the UH-60A Airloads Aircraft", American Helicopter Society 50th Annual Forum, May 1994.

[4] Johnson, W., "Technology Drivers in the Development of CAMRAD II", American Helicopter Society Aeromechanics Specialist Meeting, San Francisco, CA, January 19-21, 1994.

[5] Yeo, H., Bousman, W.G., and Johnson, W., "Performance Analysis of a Utility Helicopter with Standard and Advanced Rotor", *Journal of the American Helicopter Society*, Vol. 49, No. 3, July 2004, pp. 250–270.

[6] Shinoda, P.M., Yeo, H., and Norman, T.R., "Rotor Performance of a UH-60 Rotor System in the NASA Ames 80- by 120-Foot Wind Tunnel", *Journal of the American Helicopter Society*, Vol. 49, No. 4, October 2004.

[7] Yeo, H., and Johnson, W., "Assessment of Comprehensive Analysis Calculation of Airloads on Helicopter Rotors", *Journal of Aircraft*, Vol. 42, No. 5, September–October 2005.

[8] Yeo, H., and Johnson, W., "Prediction of Rotor Structural Loads with Comprehensive Analysis", *Journal of the American Helicopter Society*, Vol. 53, No. 2, April 2008.

[9] Yeo, H., Romander, E., and Norman, T., "Investigation of Rotor Performance and Loads of a UH-60A Individual Blade Control System", American Helicopter Society 66th Annual Forum, Phoenix, AZ, May 11–13, 2010.

[10] Yeo, H., Bousman, W.G., and Johnson, W., "Performance Analysis of a Utility Helicopter

with Standard and Advanced Rotor", *Journal of the American Helicopter Society*, Vol. 49, No. 3, July 2004, pp. 250–270.

[11] Buning, P.G., Gomez, R.J., and Scallion, W.I., "CFD Approaches for Simulation of Wing-Body Stage Separation", AIAA-2004-4838, AIAA 22nd Applied Aerodynamics Conference, Providence, RI, August 16–19,2004.

[12] Potsdam, M., Strawn, R.C., and Meakin, R., "Dynamic Rotorcraft Applications Using Overset Grids", 31st European Rotorcraft Forum, Florence, Italy, September 13–15, 2005.

[13] Tung, C., Caradonna, F.X., and Johnson, W., "The Prediction of Transonic Flows on an Advancing Rotor", American Helicopter Society 40th Annual Forum, Arlington, VA, May 16–18, 1984.

[14] Potsdam, M., Yeo, H., and Johnson, W., "Rotor Airloads Prediction Using Loose Aerodynamic/Structural Coupling", *Journal of Aircraft*, Vol. 43, No. 3, May–June 2006.

[15] Nygaard, T., Saberi, H., Ormiston, R.A., Strawn, R.C., and Potsdam, M., "CFD and CSD Coupling Algorithms and Fluid Structure Interface for Rotorcraft Aeromechanics in Steady and Transient Flight Conditions", American Helicopter Society 62nd Annual Forum, Phoenix, AZ, May 9–11, 2006.

[16] Chang, I-C., et al., "Airloads Prediction of a UH-60A Rotor Inside The 40- by 80-Foot Wind Tunnel", American Helicopter Society Specialists' Conference on Aeromechanics, San Francisco, CA, January 20–22, 2010.